International Journal of Hydrogen Energy 144 (2025) 124–132

Contents lists available at ScienceDirect

International Journal of Hydrogen Energy

journal homepage: www.elsevier.com/locate/he

Electrochemical performance of Ni–Fe–Co spinel anodes with a nanorod structure in anion exchange membrane water electrolyzers

Ataollah Niyati, Arianna Moranda, Ombretta Paladino *

Department of Civil, Chemical and Environmental Engineering, University of Genoa, Via Opera Pia 15, 16145, Genoa, Italy

ARTICLE INFO

Handling Editor: Fanglin F. Chen

Keywords:
Anion exchange membrane water electrolysis
Alkaline water electrolysis
Green hydrogen production
Oxygen evolution reaction
Ni–Fe–Co nanorod spinel
Metal oxide electrocatalyst

ABSTRACT

Green hydrogen production via anion exchange membrane water electrolyzers (AEMWEs) is becoming a game changer as a sustainable energy solution by offering a cost-effective alternative to conventional electrolyzers. In this study, Ni–Fe–Co spinel electrocatalysts, with a specific nanorod morphology engineered to optimize ion diffusion, were synthesized via a sono-hydrothermal method and evaluated as anodes in AEMWEs. Four different compositions of nanostructured Ni–Fe–Co oxides, all based on the $NiCo_2O_4$ spinel, and named NiCo3–S, NiCo4–S, NiFe1–S (10 % Fe), and NiFe2–S (20 % Fe) were synthesized and spray-coated onto nickel felt gas diffusion layers. A Pt/C cathode and an Aemion + membrane completed the 5 cm^2 AEMWE assembly. The structural analysis confirmed well-defined spinel phases and a nanorod morphology for all the electrocatalysts, with NiFe2–S exhibiting enhanced crystallinity and smaller nanorod dimensions. Electrochemical tests revealed that AEM cells equipped with NiFe2–S anodes achieved a low cell voltage of 1.808 V at 1 A. cm^{-2} and 2.06 V at 2 A. cm^{-2}, outperforming other electrocatalysts. A 45-h DC stability test showed only a slight voltage increase (1.815 V–1.866 V), while a 20-h accelerated stress test (AST) confirmed minimal degradation. These results demonstrate that Fe incorporation inside an already optimized nanorod structure improves electrocatalytic activity, charge transfer, and durability, making NiFe2–S a promising anode material for scalable AEMWE applications, further advancing the development of cost-effective green hydrogen production.

1. Introduction

Water electrolysis is a highly efficient and sustainable technology for producing green hydrogen in a world that is intensifying its efforts to transition toward renewable energy and as a solution for reducing carbon dioxide by industries and energy systems [1–4]. Producing green hydrogen by anion exchange membrane water electrolyzers (AEMWEs) brings some interesting benefits for splitting water into hydrogen and oxygen in comparison to conventional alkaline water electrolyzers (AWEs), such as using no or less platinum group metals in the cathode and having higher current densities [5–10]. However, a drawback holds AEMWEs back from becoming widely used, as there is still a need to figure out how to engineer oxygen evolution reaction (OER) catalysts that are both highly effective and tough enough to last a long time under real-world conditions. Solving this durability could reveal their full potential in sustainable energy production for having a clean environment [11–15]. As an active part of an electrolyzer in which water splitting happens, transition metal-based electrocatalysts offer a cost-effective option for AEMWE electrodes, while maintaining high performance, enabling the achievement of higher current densities without relying on expensive noble metals [16–19].

Among the various non-precious metal-based electrocatalysts studied for OER, spinel-type transition metal oxides have gained prominence due to their tunable electronic properties, multiple oxidation states, and high intrinsic stability in alkaline media [20–23]. Spinel oxides, specifically Ni and Co spinels with the primary composition as $NiCo_2O_4$, are well known for their OER activity by providing a unique structural framework that facilitates efficient charge transfer and oxygen adsorption [24–27]. However, despite the promising characteristics of $NiCo_2O_4$, conventional spinel oxides often suffer from moderate conductivity and limited active surface area, which can restrict their overall electrocatalytic performance [28,29]. One approach for improving the electrochemical activity of $NiCo_2O_4$ for OER and especially for AEMWE would be doping of metal ions, or incorporation of these ions inside the lattice parameters, such as W-doped $NiCo_2O_4$ [4], Ce– $NiCo_2O_4$ [30], Fe ion doped $NiCo_2O_4$ [31], and Mn-doped $NiCo_2O_{4-\delta}$ [32]; in which the OER activity can be enhanced through morphological tuning and composition optimization. Hydrothermal synthesis is a promising

* Corresponding author.
E-mail address: paladino@unige.it (O. Paladino).

https://doi.org/10.1016/j.ijhydene.2025.06.018
Received 22 March 2025; Received in revised form 20 May 2025; Accepted 1 June 2025
Available online 6 June 2025

technology for achieving particles of desired shape, which can lead to interesting performance in AEMWE, as demonstrated by Ni $(OH)_2$@FeOOH and Ni_2P@$Fe_2P_2O_7$ (1 A cm^{-2} at 1.84 V) [33], $NiFe_2O_4$ (1.2 A cm^{-2} at 1.8 V) [34], h-$NiFeMoO_x$ (current density of 1000 mA cm^{-2} at voltages of 1.83 and 1.56 V at 25 and 80 °C) [35]. In general, Fe incorporation improves the redox properties and electronic conductivity of the catalyst [36]. Another approach to enhance the catalyst performance is to work on optimizing ion transport; this means to synthesize spinel catalysts with particular nanoshaped structures, which can provide a higher density of active sites and improved electron transport pathways by offering faster charge transport and better accessibility of active sites [37–39].

In this study, we adopted both the described approaches and synthesized Ni–Fe–Co spinel nanorod electrocatalysts with the sono-hydrothermal method assisted by urea and tested them as anodes inside AEMWE cells with a dry cathode configuration. The uniqueness of this work is not only associated with having an electrocatalyst with a single morphology of the nanorod structure, obtained using chloride precursor (Ni^{2+}, Co^{2+}, and Fe^{2+}) and optimizing process conditions, but also with the evaluation of their performance inside the AEMWE near industrial operating conditions. We used four different powders to prepare the anodes in which two of them had the $NiCo_2O_4$ spinel structure with small shape differences due to the choice of calcination temperature (NiCo3–S, NiCo4–S), while the other two had Fe inside the lattice of $NiCo_2O_4$ (10 %: NiFe1–S and 20 % NiFe2–S). The catalysts were deposited onto nickel felt gas diffusion layers (GDLs) using a spray-coating technique as a conventional method, while the cathode was Pt/C with 0.5 mg of Pt loading. A combination of X-ray diffraction (XRD), scanning electron microscopy (SEM), and transmission electron microscopy (TEM) were used to analyze the structural and morphological properties of the electrocatalysts; electrochemical performance was evaluated through both three-electrode (1 cm^2 active area electrode) and full-cell AEMWE testing (5 cm^2 active area cell). After assessing the best anode in AEMWE through the galvanostatic polarization curve (PL), the best anode underwent further durability and stability tests, including a 45-h DC stability test at 1 A. cm^{-2} to determine long-term operational robustness. Furthermore, an accelerated stress test (AST) was performed over 20 h, subjecting the AEMWE to repeated current fluctuations between 1 A. cm^{-2} and 0.05 A. cm^{-2} to simulate dynamic load conditions and assess degradation resistance through measuring high-frequency resistance (HFR) every 4 h. This study can uncover previously unrecognized benefits of $NiCo_2O_4$ and, more importantly, Fe incorporated $NiCo_2O_4$ nanorod anodes in AEMWEs, particularly under long-term operation, by evaluating their electrochemical performances through AST and DC stability tests at current densities ranging from 50 A cm^{-2} to 2 A cm^{-2} near realistic operating conditions.

2. Experimental

2.1. Materials

To synthesize Ni–Fe–Co mixed metal oxide electrocatalysts, $NiCl_2.6H_2O$ (99 % purity), $FeCl_2.4H_2O$ (99 % purity), $CoCl_2.6H_2O$ (98 % purity), and Urea (99 % purity) were purchased from Carlo Erba (Italy). For electrolyte preparation KOH (99 % purity) pellets were also sourced from Carlo Erba (Italy). The ion exchange membrane mounted inside the AEMWE was Aemion+® AF3-HWK9-75-X (thickness: 75 μm; IEC: 1.9–2.7 meq/g, ASR: <190 mΩ cm^2; Delivery state counter ion: Cl^-/I^-; Reinforcement: Woven PEEK [40]), as well as ionomers (Ionomr Innovations Inc., Canada). For the fabrication of the cathode, Pt/C powder (CARE-E 30 %Pt) was supplied by Cabro S.p.A.(Italy). Ethanol (EtOH) and 2-propanol (IPA) used for electrocatalyst ink preparation were purchased from Sigma Aldrich (Germany). Gas diffusion layers (GLDs) in all AEMWE were Ni felts (1 mm thickness, porosity 0.85), supplied from QL Metal Fiber Co., Ltd. (China).

2.2. Ni–Fe–Co mixed metal oxide spinel electrodes preparation

All four electrocatalysts used in this study have a spinel structure with the general formula AB_2O_4, where A and B are Ni- and Co-based metals. $NiCo_2O_4$ powder was synthesized under different calcination conditions and designated as NiCo3–S and NiCo4–S. The synthesis followed a sono-hydrothermal method using urea as a hydrolysis agent in which the pH during the synthesis was indirectly controlled by adjusting the urea-to-precursor (UTP) ratio. A value of UTP equal to 10:1, corresponds to pH around 10 and promotes the formation of NiOOH and CoOOH intermediates, leading to homogeneous nanorod structures; a lower UTP ratio as 2:1 (with a corresponding pH near 7) leads to a less uniform morphology as described in our previous studies [41–43].

For the synthesis of nanorod spinel oxide based on $NiCo_2O_4$ structure, 1.008 g of $NiCl_2{\cdot}6H_2O$ precursor was dissolved in 15 mL of deionized (DI) water and gradually added dropwise to a separate solution of 2.017 g $CoCl_2{\cdot}6H_2O$ in 20 mL of DI water. After both salts of Ni and Co were dissolved by having a transparent solution appearance, urea as a hydrolysis agent at a 1:10 M ratio of the catalyst was added, and the mixture of Ni, Co, and Urea was vigorously stirred for 40 min. To enhance nucleation and nanoparticle formation, the solution was sonicated at 110 W for an additional 40 min, and the final mixture was transferred into a 50 mL Teflon-lined stainless-steel autoclave, which was subjected to hydrothermal treatment at 125 °C for 12 h. After the sono-hydrothermal reaction, the $NiCo_2O_4$ was thoroughly washed with DI water and ethanol, filtered, and dried in a vacuum oven at 70 °C. Finally, the dried material underwent thermal treatment by calcination: NiCo3–S was calcined at 380 °C for 3 h, while NiCo4–S was treated at 430 °C for 3 h, both with a controlled heating rate of 10 °C/min. NiFe1–S and NiFe2–S were synthesized following the same procedure as NiCo4–S, except $FeCl_2{\cdot}4H_2O$ partially replaced Ni, with a 10 % molar substitution in NiFe1–S and a 20 % substitution in NiFe2–S within the spinel structure.

2.3. Spray-coating preparation of electrode

Before spraying catalyst inks, NiFelts were washed with acid to remove any impurities and oxide layers. To do this, Nifelts were immersed in 3 M HCl for 15 min and then rinsed with Acetone and DI (50 %–50 %) and sonicated for 30 min. The anode consists of synthesized powder sprayed on the NiFelt as gas diffusion layers (GDLs). Accordingly, the catalyst inks were made by dispersing NiCo3–S, NiCo4–S, NiFe1–S, or NiFe2–S in a mixture of ethanol and water (1:1 vol ratio) along with Aemion+® AP3-HNN9-00-X ionomer, maintaining a catalyst-to-ionomer weight ratio of 10:1 with the catalyst concentration to be adjusted to 5 mg/mL as the standard method for AEMWE [44–46]. The solution was subjected to sonication for 1 h to ensure homogeneity before application. The ink was sprayed by hand onto GDLs using a spray gun equipped with a 0.5 mm nozzle (FE-134K aerograph plus FD-186 compressor, Fengda) while maintaining a substrate temperature of 85 °C on a heated magnetic plate and using compressed air at 1.5 bar as the carrier gas. The final catalyst loading was controlled by regulating the volume of the sprayed dispersion, ensuring a deposition of 5 mg/cm^2, which was verified gravimetrically by measuring the electrode mass before and after coating [47]. To be more precise, ink was kept under continuous sonication during the spraying process; this precaution ensured a homogeneous distribution of catalyst particles and prevented precipitation or agglomeration within the ink. Additionally, after each electrode preparation, three-electrode measurements were performed for each newly prepared electrode, ensuring reproducibility (less than 2 % overpotential deviation) with those prepared in previous steps using the same method.

Pt/C ink was prepared following the same methodology, with a catalyst-to-ionomer weight ratio of 10:2 and a catalyst concentration of 1 mg/mL. It was sprayed similarly, with a Pt mass loading adjusted to 0.5 mg_{Pt}/cm^2 [47].

2.4. Physicochemical characterization of materials

The structural and morphological characteristics of synthesized electrocatalysts were studied for NiCo3–S, NiCo4–S, NiFe1–S, and NiFe2–S in powder form in order to grasp their behaviour. To do so, we started by taking X-ray diffraction (XRD) patterns, collected at room temperature in ambient air, utilizing a PANalytical AERIS diffractometer. XRD can make it possible to identify the crystalline phases and evaluate the overall structural properties. Meanwhile, we examined the surface morphology and microstructure using both SEM imaging, which was performed with a TESCAN microscope, and also high-resolution TEM (HRTEM) by using a JEM 2100 Plus by JEOL Ltd.

2.5. AEMWE single cell assembly

After preparation by spraying of both the anode and cathode, the anion exchange membrane water electrolyzer (AEMWE) single cells were mounted with a 5 cm^2 active area using a Dioxide Material cell assembly. Corrosion-resistant nickel plates with patterned flow fields served as bipolar plates in the cell. The core part of the cell is the membrane electrode assembly (MEA) consisting of the Aemion+® AF3-HWK9-75-X membrane (maintained in a hydrated state to preserve their ionic conductivity by immersing in KOH for at least 24 h), the anode, and the cathode. By using Polytetrafluoroethylene (PTFE) spacers in each electrode compartment, appropriate compression of the GDLs (approximately 20 % ± 5 % compression) is assured to achieve near zero-gap configuration. This compression can further minimize resistance and consequently enhance electrochemical performances [7,13]. Meanwhile, spray-coated Pt/C served as the cathode, while NiCo3–S, NiCo4–S, NiFe1–S, and NiFe2–S metal oxides functioned as the anode catalysts. From herein, each AEMWE cell test is named corresponding to the anode name, and the AEMWE cell tests of NiCo3–S vs. Pt/C, NiCo4–S vs. Pt/C, NiFe1–S vs. Pt/C, and NiFe2–S vs. Pt/C named NiCo3, NiCo4, NiFe-(10 %) and NiFe-(20 %), respectively.

2.6. Electrochemical performances and measurements

For a three-electrode configuration test, electrochemical measurements were conducted using a Vertex.10A potentiostat (Ivium Technologies B.V., Netherlands) within a 1 M KOH electrolyte. Three electrode measurements can give the initial idea about the performances of the single electrode before mounting it inside the AEMWE cell. The working electrodes, each with an exposed area of 1 cm × 1 cm, included NiCo3–S, NiCo4–S, NiFe1–S, or NiFe2–S, sprayed with ionomer on Nifelt. A Hg/HgO electrode (1 M KOH) was used as the reference, while Pt foil served as the counter electrode. To ensure consistency in potential measurements, all values referenced to Hg/HgO were converted to the reversible hydrogen electrode (RHE) scale using equation (1), with 100 % iR_s compensation applied to correct for resistance-related errors:

$$E_{(RHE)} = E_{(Hg/HgO)} + 0.927V - iR_s E_{(RHE)} = E_{(Hg/HgO)} + 0.927V - iR_s \quad (1)$$

Backward linear sweep voltammetry (BLSV) was carried out in the potential window of 1.0–1.7 V vs. RHE, employing a scan rate of 5 mV/s. Additionally, electrochemical impedance spectroscopy (EIS) was performed over a frequency range spanning 0.01 Hz to 100 kHz, at 0.6 V vs. Hg/HgO. The obtained impedance spectra were analyzed using an equivalent circuit model, where the solution resistance (R_s) was extracted for further calculations.

When it comes to testing the AEMWE single cell, the tests were performed using a VSP-300 potentiostat (Biologic, France) with an external 20 A booster. The protocol in this study consists of pretreatment of the cell for about 3–4 h, starting by warming up the electrolyte up to 60 °C ± 1.5 °C, pumping the electrolyte to the anode part, and raising the cell temperature gradually up to 60 °C. Then, the open circuit voltage (OCV) was observed for possible leakage and short circuits before activating the electrode and MEA. For activation of the MEA, cyclic voltammetry (CV) was performed from 0 to 2.5 V at a scan rate of 50 mV s^{-1} for 30 cycle numbers and after that, the AEMWE was kept under 250 mA cm^{-1} of current density for 2 h. Galvanostatic polarization curves (PL) were recorded using a multistep chrono-potentiometry (CP) method, where the current density was systematically increased from 50 mA.cm^{-2} to 2.5 mA cm^{-2}, with each step maintained for 3 min to minimize capacitive influences and the reported polarization curve values were obtained by averaging the cell voltage over the final minute of each current step. EIS was performed with 1 A cm^{-2} of current density with 50 mA of perturbation between 100 kHz and 100 mHz in which the high-frequency resistance (HFR) is allocated to the MEA resistance is shown for comparison.

A DC stability test was conducted after pretreatment and the first PL by running the AEMWE at 1 A cm^{-2} for 45 h to assess long-term performance. Additionally, a 20-h accelerated stress test (AST) was performed by alternating current density between 1 A cm^{-2} and 0.05 A cm^{-2} every 15 min and measuring HFR each 4 h, completing 40 cycles over the test period. This approach simulates rapid current fluctuations, allowing for the evaluation of electrode durability under dynamic operating conditions. It should be emphasized that all reported data for AEMWE are presented without HFR correction, ensuring that the results reflect realistic operating conditions relevant to industrial applications.

3. Results and discussion

3.1. Physicochemical characterization of materials

The physicochemical characterization of powder electrocatalysts was evaluated using XRD, SEM, and HRTEM to get a solid understanding of structure and morphology and the results are depicted in Fig. 1.

XRD spectra (Fig. 1 (a)) were taken for NiCo3–S, NiCo4–S, NiFe1–S, and NiFe2–S between 2θ of 15–75° and all of them are aligned with JCPDS No 20–0781 at 18.90°, 31.15°, 36.70°,

38.40°, 44.62°, 55.43°, 59.09°, 64.98°, and 77.54° which correspond to the (111), (220), (311),

(222), (400), (422), (511), (440), and (533) crystallographic planes of $NiCo_2O_4$. XRD analysis proved that the synthesized electrocatalysts are single-phase and have a crystalline structure that makes them suitable for water splitting, especially in AEMWE.

Although the XRD is a must-characterization technique and can reveal valuable features of the synthesized electrocatalysts, other characterization are important in terms of morphology. Accordingly, SEM and HRTEM analyses were performed as a morphology characterization technique. Fig. 1 (b) and (c) show the SEM analysis for NiCo3–S and NiCo4–S, respectively. It can be seen that the structure is nanorod with the desired dimension, with no observation of second morphology, revealing a clear success of our optimized sono-hydrothermal synthesis process using urea as a hydrolysis agent which can facilitate nucleation of nanorods over time. To go further, HRTEM analysis of NiCo4–S as an example was investigated and shown in Fig. 1(d), which demonstrates lattice spacing of 0.247 nm related to the (311) plane of $NiCo_2O_4$ spinel electrocatalyst, confirming further what was obtained by SEM and XRD analysis and revealing the purity of the synthesized samples with nano dimension. Moreover, NiFe1–S (Fig. 1(e)) and NiFe2–S (Fig. 1(f)), which have Fe inside the lattice show smaller nanorods and well distribution of catalyst growth without losing the nanorod shape as Fe is inserted inside the lattice of $NiCo_2O_4$. (EDS analysis of the NiFe2–S is given in Figs. 1(S) and 2S (Supporting Information) for the distribution of elements in the spinel structure).

3.2. Evaluation of electrodes in standard three-electrode setup

After physicochemical characterizations, the synthesized NiCo3–S, NiCo4–S, NiFe1–S, and NiFe2–S electrocatalysts, sprayed on Ni Felt, underwent three-electrode cell measurements, which can reveal their

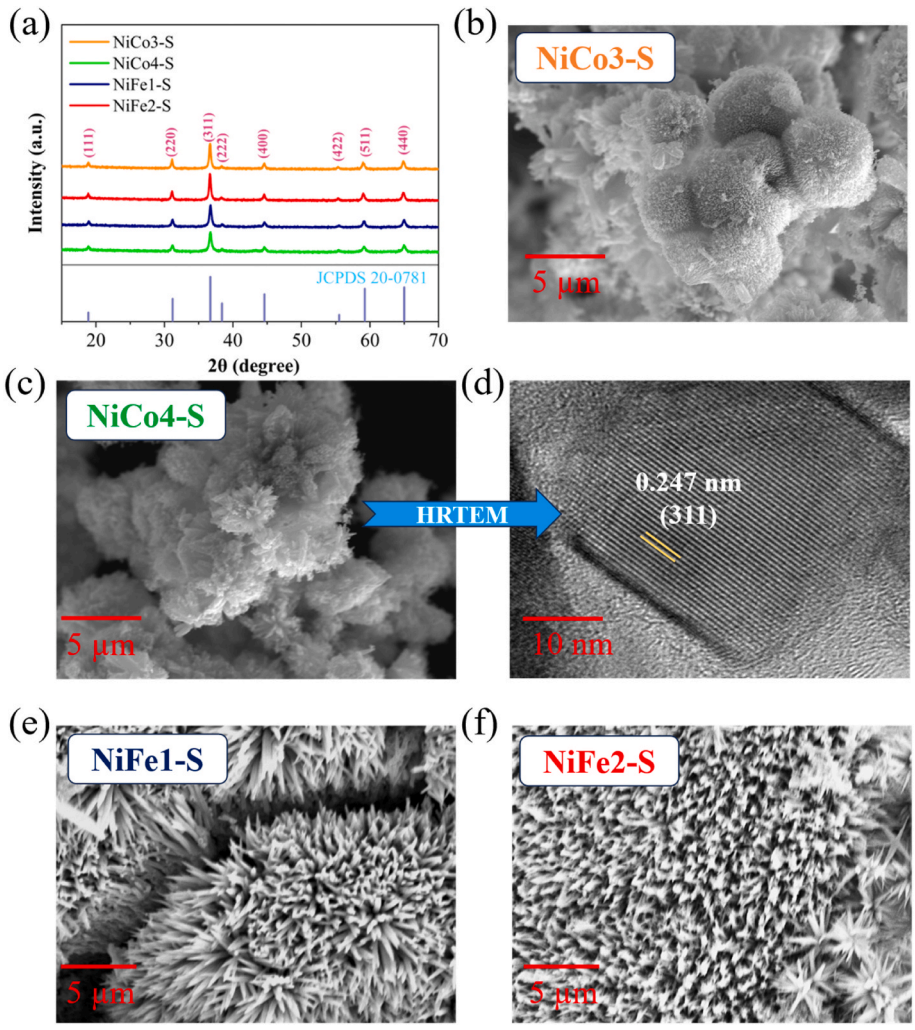

Fig. 1. Physicochemical Characterization of NiCo3–S, NiCo4–S, NiFe1–S and NiFe2–S: (a) XRD analysis; (b) SEM analysis of NiCo3–S Powder; (c) SEM analysis of NiCo4–S Powder; (d) HRTEM analysis of NiCo4–S Powder; (e) SEM analysis of NiFe1–S Powder; (f) SEM analysis of NiFe2–S Powder.

electrochemical activity for the oxygen evolution reaction (OER) before assembling the synthesized Ni–Fe–Co electrodes into the AEMWE single cells.

The linear sweep voltammetry (LSV) data, fully corrected for iR_s losses (100 %), are displayed in Fig. 2(a). All in all, all the electrocatalysts are active for OER as anode while NiFe2–S is the most active electrode standing behind the NiFe1–S, NiCo3–S, and NiCo4–S, confirming the results obtained by SEM and TEM in which highly crystalline and nanorod structure of NiFe2–S with 20 % of Fe inside the structure can enhance the electrochemical activity. For instance, by considering the current density of 50 mA cm^{-2}, NiCo3–S, NiCo4–S, NiFe1–S, or NiFe2–S require a potential of 1.629, 1,615, 1.606, and 1.593 V vs. RHE, respectively. For better comparison, overpotentials of NiCo3–S, NiCo4–S, NiFe1–S, or NiFe2–S are calculated and depicted in Fig. 2(b) at 10, 50, and 100 mA cm^{-2}. Results of overpotentials demonstrate that at lower current densities, all four electrodes are performing the same with just a maximum 6 % difference in lower current density and a maximum of 13 % in higher current densities, making them reliable electrodes for AEMWE, while at higher current densities where it is crucial for industrial AEMWE, NiFe2–S decisively performs better. Qi et al. [48] reported an overpotential of 328 mV for porous NiFeOx in 1 M KOH at 10 mA cm^{-2}, while their NiFe oxide nanorod arrays exhibited 380 mV at 5 mA cm^{-2}. Similarly, Ullah et al. [49] investigated Ni–NiO@3DHPG, Co–CoO@3DHPG, and 3DHPG synthesized via ion exchange/activation, achieving overpotentials of 1.52, 1.59, and 1.67 V (vs RHE) at 10 mA cm^{-2}, respectively. Bejar et al. [50] compared $NiCo_2O_4$ and Co_3O_4, obtaining overpotentials of 1.54 and 1.57 V (vs RHE) in 1 M KOH at 10 mA cm^{-2}. Li et al. [51] evaluated various electrocatalysts, including Co_3O_4 (370 mV), $CoMoO_4$ (340 mV), and RuO_2 (312 mV) in 1 M KOH at 10 mA cm^{-2}; with their best material, Fe–$CoMoO_4$-0.2, showing a significantly lower overpotential of 274 mV. Notably, our catalyst achieves an overpotential of just 306 mV, demonstrating competitive performance compared to both noble and non-noble catalysts.

To investigate the electrical transport properties of the electrodes, we carried out electrochemical impedance spectroscopy (EIS) at about 0.6 V vs. Hg/HgO where the current density is at around 10 mA cm^{-2} for each electrode in this study. The resulting Nyquist plots, fitted to an equivalent circuit, are presented in Fig. 2(c). The solution resistance (Rs), which is used for iR_s correction, was 0.492, 0.456, 0.529, and 0.451 Ω at 100 kHz for NiCo3–S, NiCo4–S, NiFe1–S, and NiFe2–S, respectively. As all electrocatalysts are based on spinel $NiCo_2O_4$ nanorod electrocatalyst, the semicircle shape is similar but with different charge transfer resistance (Rct) that plays a significant role in the electrochemical activity. R_{ct} determined from the semicircle diameter in the plots was 1.42, 1.359, 1.25, and 1.22 Ω for NiCo3–S, NiCo4–S, NiFe1–S, and NiFe2–S, respectively.

Tafel slopes, which shed light on OER kinetics and mechanisms, are shown in Fig. 2(d) and again confirm the better performances of NiFe2–S in comparison to its pioneering electrocatalysts. While the Tafel slope for NiFe2–S was 83.6 mV/dec, NiCo3–S, NiCo4–S, and NiFe1–S achieved

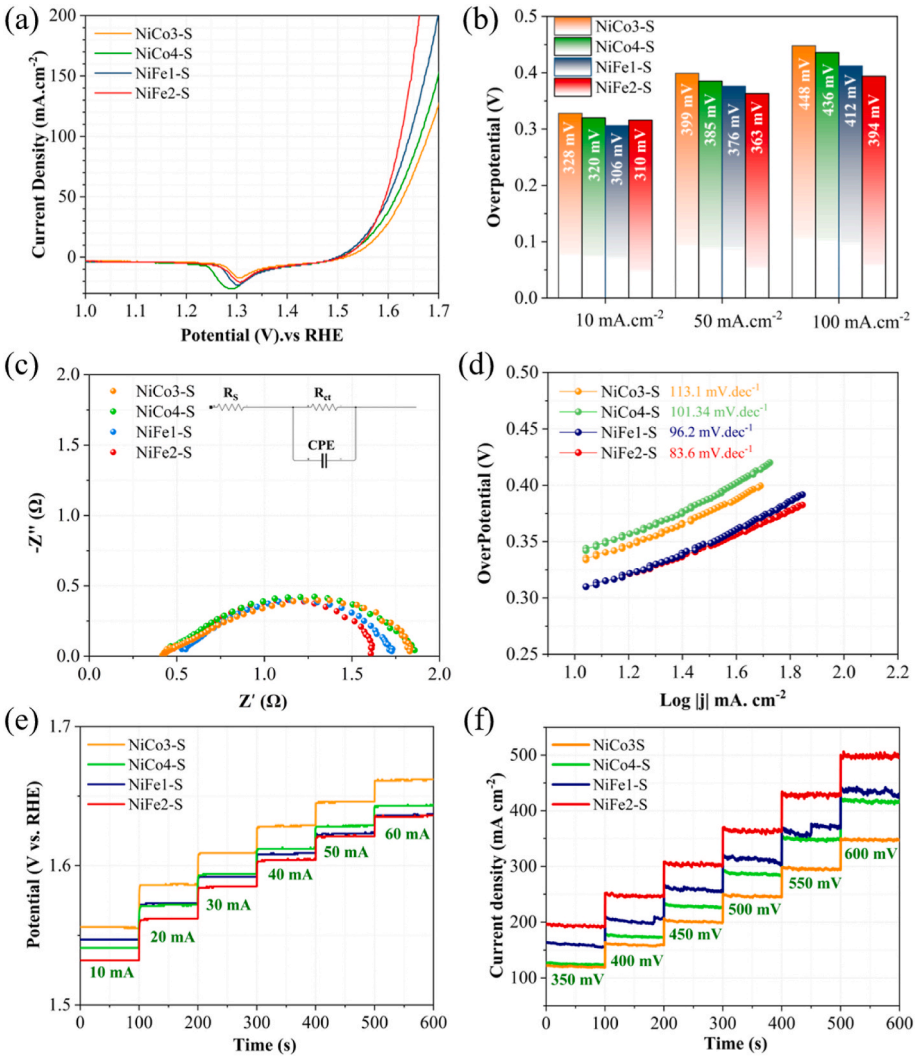

Fig. 2. Three-Electrode cell measurements for NiCo3–S, NiCo4–S, NiFe1–S, and NiFe2–S: (a) backward LSV scans with 5 mv/s; (b) comparison of the overpotentials measured at 10, 50, and 100 A cm^{-2} of current density; (c) EIS analysis at 10 mA cm^{-2}; (d) Tafel slope; (e) Chronopotentiometry test at various current densities; (f) Chronoamperometry test at various electrode potentials.

113.1, 101.3 and 96.2 mV/dec, respectively. The lower slope for NiFe2–S suggests it accelerates OER with a reduced energy barrier compared to the others.

We also assessed the short-term stability of NiCo3–S, NiCo4–S, NiFe1–S, and NiFe2–S using chronopotentiometry (CP) and chronoamperometry (CA) protocols without iR correction. In the CP test (Fig. 2(e)), current densities from 10 to 60 mA cm^{-2} were held for 100 s each as expected based on the prior three electrode tests and morphology analysis. NiFe2–S displayed reliable stability with lower overpotentials than others, standing as a better choice as an anode in AEMWE, especially for higher current densities. For the CA test (Fig. 2 (f)), potentials were increased from 350 to 600 mV vs. Hg/HgO in 100 s increments, revealing the stable performance for NiFe2–S at a higher voltage (600 mV vs. Hg/HgO) by achieving 514 mA cm^{-2} while for NiCo3–S, NiCo4–S and NiFe1–S the current density can achieve 341, 413, and 418 mA cm^{-2}, respectively.

All in all, comparing the results of XRD, SEM, and TEM with standard three-electrode test results, adding Fe to the lattice of NiCo2O4 can improve the electrochemical performances while keeping the structure in a nanorod shape without changing the morphology with homogeneous single shape electrocatalysts. Ni substitution with Fe inside the spinel structure can enhance electrical conductivity by having multiple oxidation states inside the electrocatalyst, including Fe^{2+} and Fe^{3+}. Moreover, the 3d orbitals of Fe can interact with Ni and Co by modifying the electronic structure as a synergistic effect, resulting in a better electrochemical activity for NiFe1–S and NiFe–2S in comparison to pure $NiCo_2O_4$ in NiCo3–S and NiCo4–S [52]. These facts lead to a faster electron transfer and improved charge transfer that is of paramount importance for OER in water splitting, making way for reliable green hydrogen production [27,53].

3.3. AEMWE electrochemical tests

Based on the previous results, it was grasped that the optimized sono-hydrothermal method assisted by urea can lead to the formation of nanorod-shaped Ni–Fe–Co electrocatalysts, which can improve OER performances, especially for AEMWE. Among the 4 different electrodes named NiCo3–S, NiCo4–S, NiFe1–S, and NiFe2–S, the NiFe2–S performed better not only in electrochemical behavior in three-electrode measurements with lower overpotential and higher stability but also with better morphology based on SEM analysis. However, the performance in the single-cell AEMWE would be slightly different as all the synthesized electrocatalysts in this study are based on the spinel structure of $NiCo_2O_4$ with just adding 10 % or 20 % iron in the structure. Thus, another important step for choosing the suitable electrode was to investigate the behavior of NiCo3–S, NiCo4–S, NiFe1–S, and NiFe2–S in

5 cm^2 AEMWE at different cell conditions.

The behavior of electrodes in AEMWE after pretreatment is shown in Fig. 3. Fig. 3(a) shows a schematic of AEMWE used in this study, which consists of the cathode (0.5 mg/cm2 loading of Pt as standard cathode for AEMWE), the anode, which are the synthesized electrocatalyst sprayed on the GDL (5–5.5 mg/cm^2 loading) and membrane (Aemion+).

Fig. 3(b) reveals the galvanostatic PL for NiCo3, NiCo4, NiFe-(10 %) and NiFe-(20 %) up to 2 A cm^{-2}. The electrolyte (1 M KOH) flow rate was adjusted to 6 ml/min to the anode side, as a dry cathode configuration, based on a balance between ensuring an effective ion transport and minimizing ohmic resistance, as well as suggested by the cell manufacturer; and also to avoid excessive pressure drop within the cell. Moreover, this flowrate demonstrated to be optimal for assuring uniform temperature inside the AEMWE, so as verified experimentally by temperature measurements (thermocouple and thermography camera, Hikmicro PS), and to efficiently remove bubbles from the anode side. As can be seen from Fig. 3, all AEMWE show reliable performance by achieving 1.95, 1.91, and 1.85 V for NiCo3, NiCo4, and NiFe-(10 %) with 1 A cm^{-2}. However, the NiFe-(20 %) showed better performance in comparison to others, achieving 1.808 V with 1 A cm^{-2} of current density inside the AEMWE, outperforming other electrodes in this study. NiFe-(20 %) goes a step further in reliable performance as at only 2.06 V it can have 2 A cm^{-2} of current density, while for NiCo3, NiCo4, and NiFe-(10 %) the voltage of the cell at 2 A cm^{-2} is 2.179, 2.15 and 2.08 V, respectively. Also, the EIS of all AEMWE cells was taken at 1 A cm^{-2} between 100 mHz and 100 kHz with 50 mA of amplitude in galvanostatic mode and results are given in Fig. 3 (c). The HFR part (100 kHz), which is more related to the MEA resistance, for NiCo3, NiCo4, NiFe-(10 %), and NiFe-(20 %) is 60, 56, 51.7, and 47.9 mΩ cm^{-2}, respectively, revealing the advantages of NiFe-(20 %) in AEMWE (The full EIS

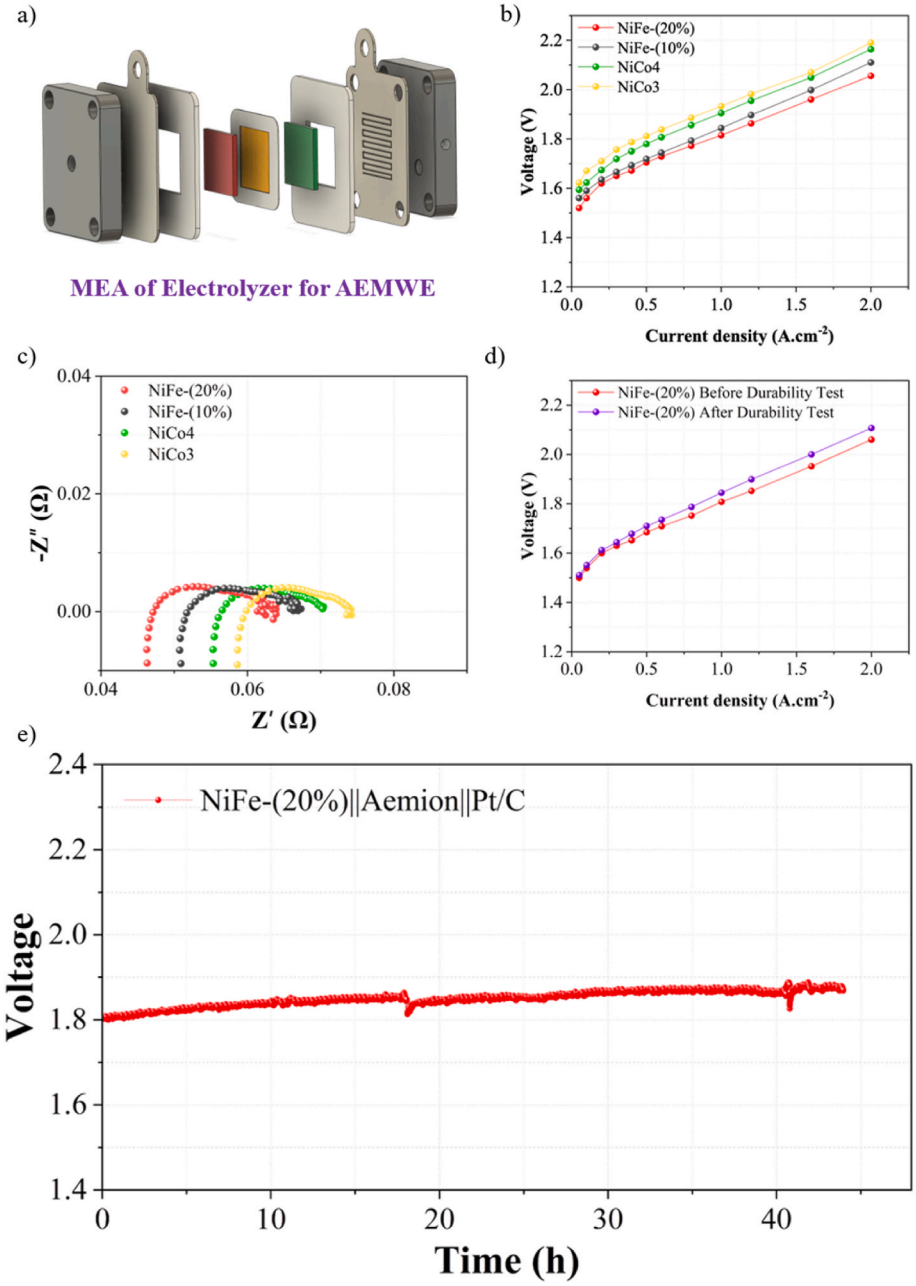

Fig. 3. The behavior of electrodes in AEMWE after Pretreatment for NiFe-(20 %), NiFe-(10 %), NiCo3, and NiCo4: (a) AEMWE schematic (b) Polarization curve for NiFe-(20 %), NiFe-(10 %), NiCo3, and NiCo4; (c) EIS at 1 A cm^{-2} for NiFe-(20 %), NiFe-(10 %), NiCo3, and NiCo4. (d) Polarization curve before and after 45 h DC test for NiFe-(20 %). (e) 45 h DC test at 1 A cm^{-2} for NiFe-(20 %).

analysis with the fitted equivalent circuit used for the extraction of HFR are provided in Supporting Information, Fig. 3(S) and Table 1S).

The initial PL curve with the results obtained from previous experiments in three-electrode tests led us to further evaluate the NiFe-(20 %) by considering a 45hr DC stability test at 1 A cm^{-2} that the results were shown in Fig. 3 (e). The Voltage of the cell starts at 1.815 V, and by a slight increase, at the end of 45 h, it is 1.866 V. We already compared the PL before and after 45 h DC tests (Fig. 3(c)), which shows that NiFe-(20 %) as AEMWE has the ability to be scaled up as even after DC test, the NiFe-(20 %) achieves 2 A cm^{-2} just by 2.107 V. As NiFe-(20 %) can even be operated with 2 A cm^{-2} after 45 h DC test in cell voltage below 2.2 V, further reveals its advantages using sono-hydrothermal method synthesis procedure in which small nuclei are shaped with using a controlled sonication power resulting in the formation of nanorod spinels that can facilitate charge transfer and improving the electrochemical activity of the NiFe2–S electrode for OER applications.

When it comes to figuring out how well an AEMWE holds up over time, especially if we want to consider possible scaling up at an industrial scale, only a DC test over time (in this study, 45-h at 1 A cm^{-2}) gives a decent preview of degradation rather than real degradation by time. When the cell is under harsh conditions over time (the AST test can simulate these conditions), dynamic challenges arise at the MEA. So, to get a better idea of the NiFe-(20 %) toughness, we put it through an AST ramping up the current density by cycling it every 15 min, mimicking harsher conditions in a shorter time frame to see how the electrode handles it.

For the AST of NiFe-(20 %), which the results are given in Fig. 4, we cycled the current density between 0.05 A cm^{-2} and 1 A cm^{-2} for 20 h without turning off the NiFe-(20 %) after 45 h DC test. Moreover, every 4 h, the HFR is measured to understand the possible degradation of the MEA over time in combination with the galvanostatic PL after the AST test. Fig. 4(a) shows the voltage of NiFe-(20 %) (in red) and HFR changes during time (in blue). The voltage at 1 A cm^{-2} at the beginning of the AST was at 1.874 V with the 205 mΩ cm^2 of the HFR per cell, while at the end of 20-hr, the voltage of cell achieved 1.886 V with HFR at around 279 mΩ cm^2. A slight fluctuation is observed after 4 h of AST test, which

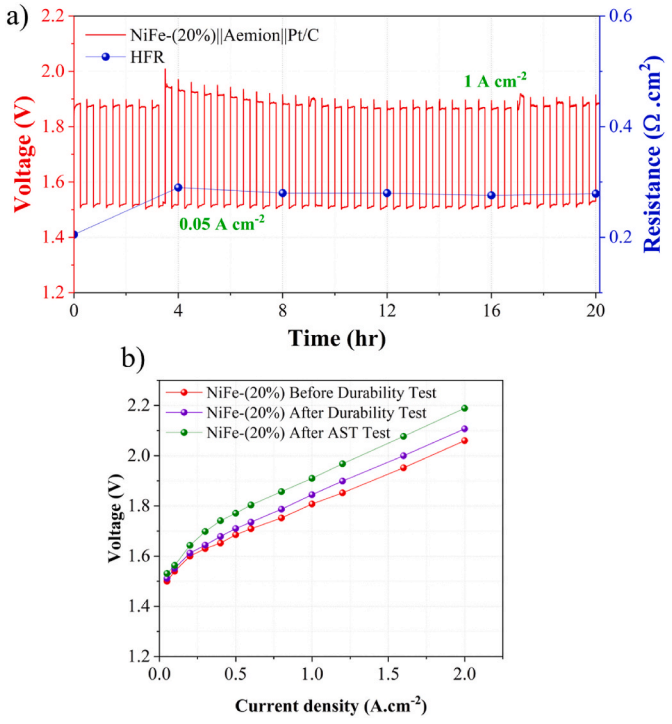

Fig. 4. NiFe-(20 %) 24-hr AST test: (a) 24-hr AST test; (b) Polarization curve Before Durability, After durability, and after AST test.

is more related to the addition of fresh electrolyte. Still, a portion of this change is attributed to the degradation of MEA and, more importantly, the leaching of active material (an increase in HFR happened at 4 h) but not in a way that can alter the performance of the cell as the cell degradation with AST is 0.6 mV h^{-1}. This is why AST can reveal some unseen behavior of the AEMWE near-real conditions. Considering 50 mA cm^{-2} current density, which does not turn off the cell but keeps it near to shut down, showed a pretty steady voltage starting from 1.529 to 1.531 V at the end of the AST.

After the AST, we ran galvanostatic PL and it is compared with the fresh, after 45 h DC test and after AST of NiFe-(20 %), and results are given in Fig. 4(b). For instance, the cell voltage operating at 1 A cm^{-2} during preconditioning, DC, and AST test showed that the voltage from 1.808 V achieved 1.845 V after 45 h of DC test and 1.899 V after 20 h AST test. The reliable part would be that even by putting the NiFe-(20 %) under harsh AST conditions, the cell voltage can be 2.107 with 2 A cm^{-2} of current density. Considering it all together, the AST showed NiFe-(20 %) is a promising cell configuration for AEMWE. After 20 h of current cycling, we saw only a slight uptick in overpotential and a small rise in HFR. This lines up with the 45-h DC test, where voltage went from 1.815 V to 1.866 V, steady enough for long-term use (The full EIS fitted data for NiFe-(20 %) are given in Table 2S, Supporting Information, from the beginning of the test up to the end of AST). For anion exchange membrane water electrolysis (AEMWE), NiFe-(20 %) stands out as a reliable pick, balancing strong OER performance (low overpotential from three-electrode tests) with the durability we need for scaling up due to the nanorod structure of the NiFe2–S synthesized with the sono-hydrothermal method. (The comparison of the synthesized electrode in this study with non-PGM and PGM electrocatalysts in AEMWE is provided in Table 3S, Supporting Information.).

Although AST tests are useful for obtaining information in a relatively short time on the durability of cell materials, these tests cannot provide complete information on long-term stability. Even if the obtained performance in AST of NiFe2–S is relevant, before using this material on an industrial scale, it is still necessary to test it on a short-stack scale.

4. Conclusions

This study demonstrates that strategic Fe incorporation into $NiCo_2O_4$ spinel with nanorod morphology, obtained with sono-hydrothermal method, significantly enhances the performance and durability of Ni–Fe–Co electrocatalyst for AEM water electrolyzers. Among the four Ni–Fe–Co anodes investigated, the one produced by spraying NiFe2–S electrocatalyst was the most promising anode, due to both the well-defined nanorod morphology and high crystallinity of the catalyst and the 20 % Fe substitution. The electrochemical evaluation revealed that NiFe2–S anode exhibits reliable OER performance in 3E tests and in full-cell AEMWE tests, in which it delivered a cell voltage of 1.808 V at 1 A cm^{-2} and 2.06 V at 2 A cm^{-2}, along with low increase in HFR by time at 100 kHz. Overall, our findings highlight the potential of NiFe2–S as a high-performance, durable anode for AEMWEs, offering a cost-effective alternative to noble metal-based catalysts by bridging the gap between fundamental material design and practical cell performance. At the actual stage of our research activity we assessed feasibility of production at a larger scale, but we have not yet carried out a detailed cost analysis for comparing this catalyst, if used as anode, with commercial available NiFe oxides. It is particularly noteworthy that the overall cost-effectiveness ratio must also take into account the fact that improving the anode materials actually allows for the choice of less noble materials on the cathode side.

CRediT authorship contribution statement

Ataollah Niyati: Writing – original draft, Methodology, Investigation, Formal analysis, Data curation, Conceptualization. **Arianna**

Moranda: Writing – review & editing, Methodology. **Ombretta Paladino:** Writing – original draft, Supervision, Project administration, Methodology, Funding acquisition, Conceptualization.

Funding

This work is partially funded by NextGeneration EU, PNRR project NEMESI (New Electrocatalysts and Membranes for Industrial-Scale Electrolyzers) and by Compagnia di San Paolo, LIFTT, POC Instrument, project ARKEL (Reactor for the production of multiscale heterostructured nanospinel Ni–Fe–Co Electrodes).

A. Niyati is supported by a PhD grant FSE+2021–2027, ESO 4.6.

Declaration of interest statement

The authors declare the following financial interests/personal relationships which may be considered as potential competing interests: Ombretta Paladino reports financial support was provided by European Union and Compagnia di San Paolo. Ataollah Niyati reports financial support was provided by Liguria Region. Other authors declare that they have no known competing financial interests or personal relationships that could have appeared to influence the work reported in this paper.

Acknowledgments

The authors wish to thank Prof. Antonio Barbucci for providing SEM and XRD analysis and Dr. Juan F. Basbus, who carried out analyses at DICCA; Prof. Antonio Comite (Head of the Elemental lab at DCCI, Department of Chemistry of the University of Genoa) and Mrs. Laura Negretti who carried out TEM analyses at DCCI. The authors also wish to thank Cabro S.p.A. for supplying their Pt/C powders for testing.

Appendix A. Supplementary data

Supplementary data to this article can be found online at https://doi.org/10.1016/j.ijhydene.2025.06.018.

References

[1] Grigoriev SA, Fateev VN, Bessarabov DG, Millet P. Current status, research trends, and challenges in water electrolysis science and technology. Int J Hydrogen Energy 2020;45:26036–58. https://doi.org/10.1016/j.ijhydene.2020.03.109.

[2] Li W, Tian H, Ma L, Wang Y, Liu X, Gao X. Low-temperature water electrolysis: fundamentals, progress, and new strategies. Mater Adv 2022;3:5598–644. https://doi.org/10.1039/D2MA00185C.

[3] Evro S, Oni BA, Tomomewo OS. Carbon neutrality and hydrogen energy systems. Int J Hydrogen Energy 2024;78:1449–67. https://doi.org/10.1016/j.ijhydene.2024.06.407.

[4] Luo J, Wang X, Gu Y, Wang S, Li Y, Wang T, et al. Hierarchical sheet-like W-doped NiCo2O4 spinel synthesized by high-valence oxyanion exchange strategy for highly efficient electrocatalytic oxygen evolution reaction. Chem. Eng. J. 2023;472:144839. https://doi.org/10.1016/j.cej.2023.144839.

[5] Xu Q, Zhang L, Zhang J, Wang J, Hu Y, Jiang H, et al. Anion exchange membrane water electrolyzer: electrode design, lab-scaled testing system and performance evaluation. EnergyChem 2022;4:100087. https://doi.org/10.1016/j.enchem.2022.100087.

[6] Ghorui UK, Sivaguru G, Teja UB, M A, Ramakrishna S, Ghosh S, et al. Anion-exchange membrane water electrolyzers for green hydrogen generation: advancement and challenges for industrial application. ACS Appl Energy Mater 2024;7:7649–76. https://doi.org/10.1021/acsaem.4c01585.

[7] Li D, Motz AR, Bae C, Fujimoto C, Yang G, Zhang F-Y, et al. Durability of anion exchange membrane water electrolyzers. Energy Environ Sci 2021;14:3393–419. https://doi.org/10.1039/D0EE04086J.

[8] Zhu J, Chen W, Poli S, Jiang T, Gerlach D, Junqueira JRC, et al. Nanostructured Fe-doped Ni $_3$ S $_2$ electrocatalyst for the oxygen evolution reaction with high stability at an industrially-relevant current density. ACS Appl Mater Interfaces 2024;16:58520–35. https://doi.org/10.1021/acsami.4c09821.

[9] Guruprasad N, van der Schaaf J, de Groot MT. Unraveling the impact of reverse currents on electrode stability in anion exchange membrane water electrolysis. J Power Sources 2024;613:234877. https://doi.org/10.1016/j.jpowsour.2024.234877.

[10] Jiang T, Jiang X, Jiang C, Wang J, Danlos Y, Liu T, et al. Novel Fe-modulating raney-Ni electrodes toward high-efficient and durable AEM water electrolyzer. Adv Energy Mater 2025. https://doi.org/10.1002/aenm.202501634.

[11] Lee J, Jung H, Park YS, Woo S, Yang J, Jang MJ, et al. High-efficiency anion-exchange membrane water electrolyzer enabled by ternary layered double hydroxide anode. Small (Weinh) 2021;17. https://doi.org/10.1002/smll.202100639.

[12] Faqeeh AH, Symes MD. A standard electrolyzer test cell design for evaluating catalysts and cell components for anion exchange membrane water electrolysis. Electrochim Acta 2023;444:142030. https://doi.org/10.1016/j.electacta.2023.142030.

[13] Chen P, Hu X. High-efficiency anion exchange membrane water electrolysis employing non-noble metal catalysts. Adv Energy Mater 2020;10. https://doi.org/10.1002/aenm.202002285.

[14] Chand K, Paladino O. Recent developments of membranes and electrocatalysts for the hydrogen production by anion exchange membrane water electrolysers: a review. Arab J Chem 2023;16. https://doi.org/10.1016/j.arabjc.2022.104451.

[15] Li Q, Molina Villarino A, Peltier CR, Macbeth AJ, Yang Y, Kim M-J, et al. Anion exchange membrane water electrolysis: the future of green hydrogen. J Phys Chem C 2023;127:7901–12. https://doi.org/10.1021/acs.jpcc.3c00319.

[16] Karthikeyan SC, Ramakrishnan S, Prabhakaran S, Subramaniam MR, Mamlouk M, Kim DH, et al. Low-cost self-reconstructed high entropy oxide as an ultra-durable OER electrocatalyst for anion exchange membrane water electrolyzer. Small (Weinh) 2024;20. https://doi.org/10.1002/smll.202402241.

[17] Wang X, Zhang H, Liang Y, Huang L, Wang H. Enhanced electrooxidation of furfural to 2-furoic acid over NiCo2O4/NF: optimization, in-situ monitoring and continuous AEM cell evaluation. Appl Catal Gen 2025;696:120169. https://doi.org/10.1016/j.apcata.2025.120169.

[18] Yang R, Fu H, Han Z, Feng G, Liu H, Gao Y, et al. Hierarchical Fe-based electrocatalyst for lattice oxygen mediated water oxidation with Industrial-Level activity. J Colloid Interface Sci 2025;686:107–17. https://doi.org/10.1016/j.jcis.2025.01.210.

[19] Riemer M, Duval-Dachary S, Bachmann TM. Environmental implications of reducing the platinum group metal loading in fuel cells and electrolysers: anion exchange membrane versus proton exchange membrane cells. Sustain Energy Technol Assessments 2023;56:103086. https://doi.org/10.1016/j.seta.2023.103086.

[20] Liu H-J, Zhang S, Fan R-Y, Liu B, Lv R-Q, Chai Y-M, et al. Activated M,S co-doping (M = Ni, Co, Mn) inverse spinel oxides with mixed mechanisms for water oxidation. Appl Catal, B 2024;343:123567. https://doi.org/10.1016/j.apcatb.2023.123567.

[21] Zheng J, Sun R, Meng D, Guo J, Wang Z. Boosting oxygen evolution reaction performance *via* metal defect-induced lattice oxygen redox reactions on spinel oxides. J Mater Chem A Mater 2023;11:15044–53. https://doi.org/10.1039/D3TA01385E.

[22] Deng Q, Li H, Pei K, Wong LW, Zheng X, Tsang CS, et al. Strategic design for high-efficiency oxygen evolution reaction (OER) catalysts by triggering lattice oxygen oxidation in cobalt spinel oxides. ACS Nano 2024;18:33718–28. https://doi.org/10.1021/acsnano.4c14158.

[23] Vinodh R, Sharanappa Kalanur S, Kumar Natarajan S, Pollet BG. Nanostructured NiMoO4 electrode materials for efficient oxygen evolution reaction. J Ind Eng Chem 2024;138:432–9. https://doi.org/10.1016/j.jiec.2024.04.022.

[24] Sultan F, Zhu J, Medina DI, Pescarmona PP, Cholula-Díaz JL, Morales DM. Nickel cobalt oxide-based heterostructures as electrocatalysts for the oxygen evolution reaction at industry-relevant conditions. Int J Hydrogen Energy 2025;114:440–51. https://doi.org/10.1016/j.ijhydene.2025.02.449.

[25] Chen R, Wang H-Y, Miao J, Yang H, Liu B. A flexible high-performance oxygen evolution electrode with three-dimensional NiCo2O4 core-shell nanowires. Nano Energy 2015;11:333–40. https://doi.org/10.1016/j.nanoen.2014.11.021.

[26] Cyril Jesudass S, Surendran S, Janani G, Kim T-H, Park Y Il, Sim U. Defect-Induced Bimetallic Cubic-Spinel NiO/NiCo2O4 heterostructures via Na-Incorporation towards efficient electrochemical water splitting performances. Appl Surf Sci 2025;688:162352. https://doi.org/10.1016/j.apsusc.2025.162352.

[27] Sarkar S, Chaubey P, Sharma PKr. Inverse spinel Fe-NiCo2O4/NiO nanocomposite supported on defect-rich P-rGO sheets for enhanced OER activity. J Alloys Compd 2025;1010:177856. https://doi.org/10.1016/j.jallcom.2024.177856.

[28] Murugan N, Thangarasu S, Seo S Bin, Mariappan A, Choi YR, Oh TH, et al. N-doped defect-rich porous carbon nanosheets framework from renewable biomass as efficient metal-free bifunctional electrocatalysts for HER and OER application. Renew Energy 2024;222:119801. https://doi.org/10.1016/j.renene.2023.119801.

[29] Nagarani S, Krishnamachari M, Kumar M, Chang J-H, Balagowtham N. Synergistic effect of Nitrogen and Boron co-doped porous actived carbon encapsulated NiCo2O4 nanosphere composite for enhanced Oxygen Eevolution Reaction. J Electroanal Chem 2025;983:119023. https://doi.org/10.1016/j.jelechem.2025.119023.

[30] Wang X, Hu J, Lu T, Wang H, Sun D, Tang Y, et al. Importing atomic rare-earth sites to activate lattice oxygen of spinel oxides for electrocatalytic oxygen evolution. Angew Chem Int Ed 2025;64. https://doi.org/10.1002/anie.202415306.

[31] Fu X, Yu J, Li H, Zhang Y, Pan S, Fu Y, et al. Fe ion doping as an effective strategy to enhance oxygen evolution reaction activity in NiCo2O4. J Power Sources 2025;630:236159. https://doi.org/10.1016/j.jpowsour.2024.236159.

[32] Zhao H, Zhu L, Yin J, Jin J, Du X, Tan L, et al. Stabilizing lattice oxygen through Mn doping in NiCo $_2$ O $_{4-\delta}$ spinel electrocatalysts for efficient and durable acid oxygen evolution. Angew Chem Int Ed 2024;63. https://doi.org/10.1002/anie.202402171.

[33] Meena A, Thangavel P, Jeong DS, Singh AN, Jana A, Im H, et al. Crystalline-amorphous interface of mesoporous Ni2P @ FePOxHy for oxygen evolution at high current density in alkaline-anion-exchange-membrane water-electrolyzer. Appl Catal, B 2022;306:121127. https://doi.org/10.1016/j.apcatb.2022.121127.

[34] Martinez-Lazaro A, Caprì A, Gatto I, Ledesma-García J, Rey-Raap N, Arenillas A, et al. NiFe2O4 hierarchical nanoparticles as electrocatalyst for anion exchange membrane water electrolysis. J Power Sources 2023;556:232417. https://doi.org/10.1016/j.jpowsour.2022.232417.
[35] Cui X, Ding Y, Tang T, Wang L, Zhang F, Li P, et al. Hierarchical NiFeMoO $_4$ precatalyst reconstructed NiFeOOH anodes for efficient and durable anion-exchange membrane water electrolysis. ACS Appl Mater Interfaces 2025. https://doi.org/10.1021/acsami.5c03491.
[36] Ruan M, Wei X, Chen H, Wang L, Li T, Wang H, et al. Promotion of oxygen evolution through the modification of Co-O bond in spinel NiCo2O4. J Phys Chem Solid 2024;189:111955. https://doi.org/10.1016/j.jpcs.2024.111955.
[37] Du X, Zhang C, Wang H, Wang Y, Zhang X. Controlled synthesis of Co9S8@NiCo2O4 nanorod arrays as binder-free electrodes for water splitting with impressive performance. J Alloys Compd 2021;885:160972. https://doi.org/10.1016/j.jallcom.2021.160972.
[38] Wang Q, Wang H, Cheng X, Fritz M, Wang D, Li H, et al. NiCo2O4@Ni2P nanorods grown on nickel nanorod arrays as a bifunctional catalyst for efficient overall water splitting. Mater Today Energy 2020;17:100490. https://doi.org/10.1016/j.mtener.2020.100490.
[39] Samantara AK, Kamila S, Ghosh A, Jena BK. Highly ordered 1D NiCo2O4 nanorods on graphene: an efficient dual-functional hybrid materials for electrochemical energy conversion and storage applications. Electrochim Acta 2018;263:147–57. https://doi.org/10.1016/j.electacta.2018.01.025.
[40] Klinger A, Strobl O, Michaels H, Kress M, Martic N, Maltenberger A, et al. Transport of hydrogen through anion exchange membranes in water electrolysis. Adv Mater Interfac 2025;12. https://doi.org/10.1002/admi.202400515.
[41] Niyati A, Moranda A, Basbus JF, Paladino O. Unlocking the potential of NiCo $_2$ O $_4$ nanocomposites: morphology modification based on urea concentration and hydrothermal and calcination temperature. New J Chem (1987) 2024;48:11035–43. https://doi.org/10.1039/D4NJ01581A.
[42] Niyati A, Moranda A, Beigzadeh Arough P, Navarra FM, Paladino O. Electrochemical performance of a hybrid NiCo2O4@NiFelt electrode at different operating temperatures and electrolyte pH. Energies 2024;17:3703. https://doi.org/10.3390/en17153703.
[43] Paladino O, Niyati A, Moranda A, Beigzadeh Arough P, Marcenaro B. Engineering potential electrocatalysts for both AEM Electrolyzers and Redox Flow Batteries: design of experiments at the different scales. Appl Therm Eng 2025;258:124532. https://doi.org/10.1016/j.applthermaleng.2024.124532.
[44] Khataee A, Shirole A, Jannasch P, Krüger A, Cornell A. Anion exchange membrane water electrolysis using Aemion^{TM} membranes and nickel electrodes. J Mater Chem A Mater 2022;10:16061–70. https://doi.org/10.1039/D2TA03291K.
[45] Fortin P, Khoza T, Cao X, Martinsen SY, Oyarce Barnett A, Holdcroft S. High-performance alkaline water electrolysis using Aemion^{TM} anion exchange membranes. J Power Sources 2020;451:227814. https://doi.org/10.1016/j.jpowsour.2020.227814.
[46] Cossar E, Murphy F, Walia J, Weck A, Baranova EA. Role of ionomers in anion exchange membrane water electrolysis: is aemion the answer for nickel-based anodes? ACS Appl Energy Mater 2022;5:9938–51. https://doi.org/10.1021/acsaem.2c01604.
[47] Faid AY, Xie L, Barnett AO, Seland F, Kirk D, Sunde S. Effect of anion exchange ionomer content on electrode performance in AEM water electrolysis. Int J Hydrogen Energy 2020;45:28272–84. https://doi.org/10.1016/j.ijhydene.2020.07.202.
[48] Qi J, Zhang W, Xiang R, Liu K, Wang H, Chen M, et al. Porous nickel–iron oxide as a highly efficient electrocatalyst for oxygen evolution reaction. Adv Sci 2015;2. https://doi.org/10.1002/advs.201500199.
[49] Ullah N, Zhao W, Lu X, Oluigbo CJ, Shah SA, Zhang M, et al. In situ growth of M-MO (M = Ni, Co) in 3D graphene as a competent bifunctional electrocatalyst for OER and HER. Electrochim Acta 2019;298:163–71. https://doi.org/10.1016/j.electacta.2018.12.053.
[50] Béjar J, Álvarez-Contreras L, Ledesma-García J, Arjona N, Arriaga LG. Electrocatalytic evaluation of Co3O4 and NiCo2O4 rosettes-like hierarchical spinel as bifunctional materials for oxygen evolution (OER) and reduction (ORR) reactions in alkaline media. J Electroanal Chem 2019;847:113190. https://doi.org/10.1016/j.jelechem.2019.113190.
[51] Li C, Yang X, Kou Y, Song H, Li X, Wu C, et al. Low-level Fe doping in CoMoO $_4$ enhances surface reconstruction and electronic modulation creating an outstanding OER electrocatalyst for water splitting. Inorg Chem 2025;64:2508–17. https://doi.org/10.1021/acs.inorgchem.4c05100.
[52] Zhang L, Fan Q, Li K, Zhang S, Ma X. First-row transition metal oxide oxygen evolution electrocatalysts: regulation strategies and mechanistic understandings. Sustain Energy Fuels 2020;4:5417–32. https://doi.org/10.1039/D0SE01087A.
[53] Peng Y, Hajiyani H, Pentcheva R. Influence of Fe and Ni doping on the OER performance at the Co $_3$ O $_4$ (001) surface: insights from DFT+ *U* calculations. ACS Catal 2021;11:5601–13. https://doi.org/10.1021/acscatal.1c00214.